Final Report of the $\bar{\text{P}}$ANDA PID TAG

Draft 0.5

G. Schepers, GSI Darmstadt, et al.

Contents

1 Introduction

The $\bar{\text{P}}$ANDA ([1]) PID TAG (Particle Identification Technical Assessment Group) was installed to give to the collaboration a complete set of parameters for an optimal set of particle detectors. The task given to this TAG is described in more detail:

Subject

- Requirements from physics
- Evaluate potential of each subsystem
- Matching of systems

Deliverables

- Definition of global PID scheme
- Optimized set of detectors and parameters

This list reflects roughly the structure of the PID TAG work and of this report. In an additional subsection the tools available for the PID TAG work are presented and explained (see also [2]) . The PID TAG evaluated the necessity of mapping the "Separation Power" in dependence of the momentum and the polar angle of the reaction products which is described in section **??**. Since a "full simulation" was not available to calculate the performance of all the sub detectors, the TAG gathered parameterizations of the single sub detectors which went into a "Fast Simulation" explained in section 4.3. For single physics channels a "Full Simulation" was used.

Amongst others some important questions to solve were:

- PID with and with out the information of a Time Projection Chamber (TPC)
- PID with and with out an Forward Endcap Cherenkov, and with different forms (Focusing Disc DIRC, Time of Propagation Disc DIRC and Proximity RICH)
- PID with and with out a Forward RICH

The PID TAG had about 10 presence meetings and over 15 on line meetings. First PID subsystems were defined. Each subsystem has its responsible representative. Each representative had a replacement of his own group to guarantee always the same level of knowledge in all subsystems. For special subjects experts were asked to present informations in the meeting or to give answers to questions which arose.

The members of the TAG and their special responsibilities are listed at the end of the document (section 9).

2 Physics Requirements

The HESR (High Energy Storage Ring) of the new FAIR (Facility for Antiproton and Ion Research) project provides an Antiproton beam of high resolution (down to $\Delta p = 1 \times 10^{-5}$) and intensity from 1.5 GeV/c to 15 GeV/c momentum.

This offers the unique possibility of investigating a broad filed of physics. The vast variety of reaction types from meson-production over Charmonium decays to Hyper nuclear reactions demands a complete and compact detector system.

The physics requirements to the detectors are:

- to cover the full angular range of the physics products
- to detect all momenta of the reaction products
- to separate particle types with a defined level of separation over the full range of momenta of the reaction products.

The full solid angle can only be covered by the full set of detectors. Sometimes the momentum coverage has to be fulfilled by a combination of two or even three sub detectors.

For the single subsystems benchmark-channels had to be identified (Table 1) and simulated.

Channel	Final state	Related to detector
$\bar{p}p \to (n)\pi^+\pi^-$	$(n)\pi^+\pi^-$	EMC
$\bar{p}p \to \psi(3770) \to D^+D^-$	$2K\,4\pi$	DIRCs, ToF
$\bar{p}p \to \eta_c \to \phi\phi$	4K	DIRCs
$\bar{p}p \to D_S D^*_{S0}(2317)$	$\pi^\pm K^+ K^-$	DIRCs
		muon
		Forward RICH

Table 1: Benchmark channels to evaluate the performance of the different PID detectors.

At $\bar{\text{P}}$ANDA 2×10^7 reactions per second with up to 10 charged particles per reaction have to be digested by the detectors.

3 PID Subsystems

The different behavior of charged particles traversing active and passive detector material can be used to identify (on a probabilistic level) the nature of a charged particle. The PID detectors used in PANDA take advantage of the following effects:

- Specific Energy Loss. The mean energy loss of charged particles per unit length, usually referred to as dE/dx, is described by the Bethe-Bloch equation which depends on the velocity rather than momentum of the charged particle.
- Cherenkov Effect. Charged particles in a medium with refractive index n propagating with velocity $\beta > 1/n$ emit radiation at an angle $\Theta_C = arccos(1/n\beta)$. Thus, the mass of the detected particle can be determined by combining the velocity information determined from Θ_C with momentum information from the tracking detectors.
- Time-of-flight. Particles with the same momentum, but different masses travel with different velocities, thus reaching a time-of-flight counter at different times relative to a common start.
- Absorption. A thick layer of passive material absorb most particles due to electromagnetic (e+e-, γ) or hadronic interactions (all charged and neutral hadrons). After a certain amount of material only muons and neutrinos survive. The muons can then be detected easily with any kind of charged particle detector, depending on the desired speed and resolution.

The group of subsystems building the particle identification system of $\bar{\text{P}}$ANDA are listed with growing distance to the Target point:

- Time Projection Chamber
- Time of Flight
- Barrel DIRC
- Barrel Calorimeter
- Forward Cherenkov
- Forward Calorimeter
- Muon Counter

3.1 Central Tracker

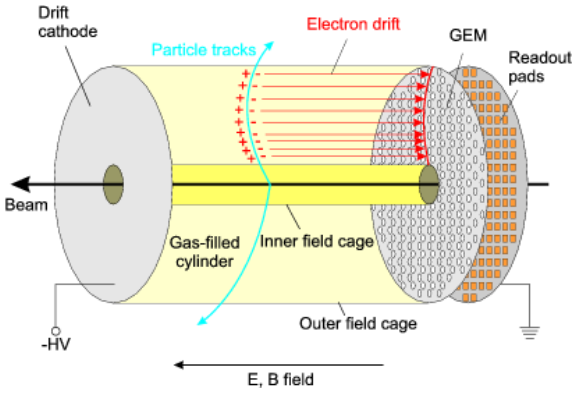

Figure 1: GEM-TPC working principle

3.1.1 Time Projection Chamber (TPC)

The TPC is discussed as a solution for the outer tracking within the target spectrometer (as Central Tracker). The required momentum resolution is ≈ 1 %, the required vertex resolution $\approx 150\ um$ in the xy plane and $< 1\ cm$ in z direction.

In addition provides the TPC in the momentum range below $\approx 1\ GeV/c$ and above $\approx 2\ GeV/c$ information for particle identification within the target spectrometer. Especially for particles with momenta below $\approx 1\ GeV/c$ this is of great help for the overall PID performance and to supplement the information from the barrel DIRC.

Working principle

General:3D tracking device - charged particles ionize detector gas - electric field along cylinder axis separates positive gas ions from electrons - primary electrons drift towards readout anode - gas amplification done by several GEM foils - ungated, continuous operation mode due to HESR beam properties - intrinsic ion feedback suppression by GEM foils - continuous data readout within PANDA DAQ - parallel online data reduction and processing (including tracking)

PID: performed via measurement of mean energy loss per track length (dE/dx), described by Bethe-Bloch-formula, in combination with (obligatory) momentum measurement - PANDA TPC offers to do $\approx 50-100$ (fluctuating) energy loss measurements per track - truncated mean algorithm used to get rid off Landau tail and to calculate mean.

Important values

Geometry: inner radius: 15 cm, outer radius: 42cm, length: 150 cm, gas volume: 700l, 2 separate chambers (due to target pipe)

Material budget: $\frac{X}{X_0} \approx 1.5$ %

Detector gas: Ne/CO2 (90/10, maybe admixture of CH4), gas gain: several 1000

Operation: drift field: 400 V/cm, 2x2 mm pads (100000)

First estimates and simulations (obtained from old PANDA framework and preliminary)

Data were generated based on an event generator which shoots p, K, pi, mu and e (plus antiparticles) isotropically through the TPC. All tracks come from the IP, with momenta between 0.2 and 4 GeV/c. Tracks are divided into 6 mm pieces, for each the energy loss is calculated resulting

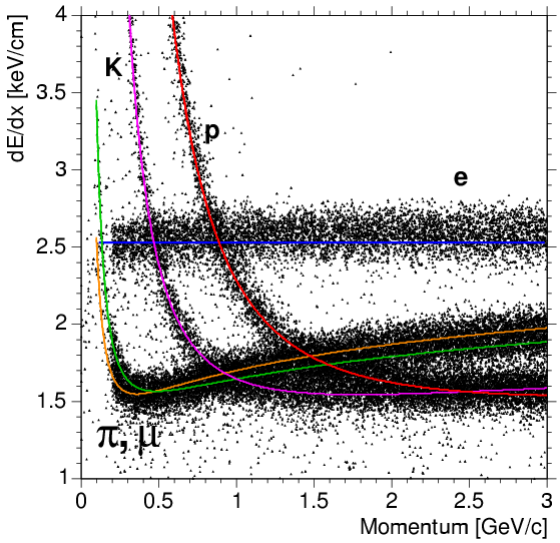

Figure 2: Energy loss in the TPC vs. momentum

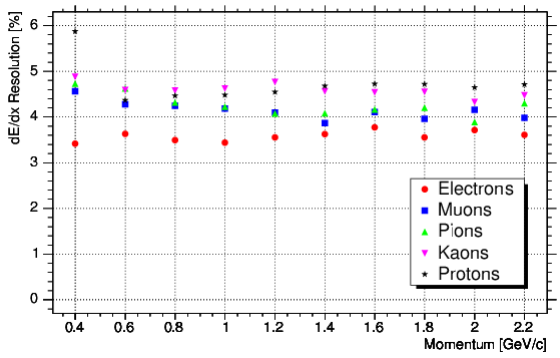

Figure 3: Energy loss resolution TPC

in 50-100 measurements depending on track length. Upper 40 % are discarded and mean dE/dx calculated (truncated mean). The spread of the these dE/dx values for certain p bins is fitted with a Gaussian and the dE/dx resolution is defined as the corresponding sigma.

The separation power between two particles is defined as:

$$\sigma_{sep} = \frac{2 * |I_1 - I_2|}{\left(\frac{\sigma(I_1)}{I_1} + \frac{\sigma(I_2)}{I_2}\right)} \tag{1}$$

where I stands for the dE/dx of the respective particle. A constant dE/dx resolution of 5% was assumed.

Note:For all the simulation results shown here the gas density value was a factor of 1.5 to high. Therefore we expect the performance to be a bit worse. For example the dE/dx resolution will change from 5% to 7%. Simulations will be repeated with the new PANDA framework as soon as possible.

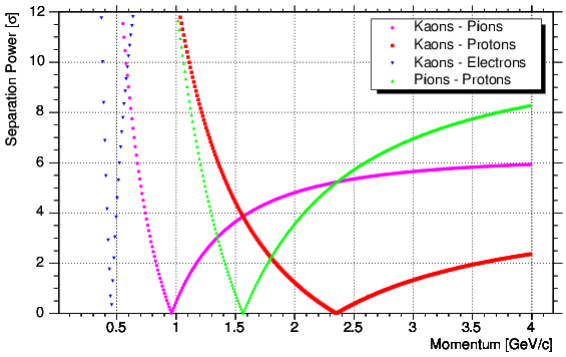

Figure 4: TPC separation power vs. momentum

3.1.2 Straw Tube Tracker (STT)

3.2 Time of Flight (ToF)

3.3 Barrel DIRC

The purpose of the Barrel DIRC (Detection of Internal Reflected Cherenkov photons) is to provide a particle identification. The mass of the particle can be achieved by combining the velocity information of the DIRC with momentum information from the tracking detectors. In addition the distinction between gammas and relativistic charged particles entering the EMC behind the DIRC is possible.

Basis for the calculations and simulations are the bar dimensions taken from the BaBar DIRC [3]. With the length adapted to the $\bar{\text{P}}$ANDA setup there are quartz bars of $17 \times 35 \times 2300\ mm^3$ and a distance of 480 mm to the target point. Thus the barrel DIRC covers the solid angle between 22 and 140 degrees. The lower momentum threshold for kaons which produce Cherenkov light is for an envisaged refractive index of n=1.47 as low as 460 MeV/c for single photon production. For larger photon numbers the threshold increases.

With 17mm (of thickness) of fused silica the DIRC bars present approximately 14% of a radiation length to normal incident particles. The support structure will add 3%.

This design is initially based on the BaBar DIRC [3] but at $\bar{\text{P}}$ANDA further improvements of the performance are under development. The combination of the spatial image of the photons with their time of arrival gives access not only to their velocity but also to the wavelength of the photons. Thus dispersion correction at the lower and upper detection threshold becomes possible. Further on the reduction of the photon readout in size and number of photon detectors is envisaged. A lens or a set of lenses at the exit of the quartz bar focus the photons to a focal plane behind a readout volume of about 30 cm length. When this volume is filled with a medium with the same refractive index as the radiator material (n_{medium}=$n_{radiator}$=1.5) additional dispersion effects and other image distortions are avoided.

A major issue is the maintenance of the barrel DIRC. While in the Babar DIRC a removal of the radiator barrel and the photon detector was not foreseen, the PANDA barrel DIRC is planned removable. The removal is not planned as default operation during maintenance breaks. Rather the access to other detector parts and the replacement of broken DIRC items need a removal procedure. For that purpose a photon detector smaller in size is favorable. The segmentation of the radiator barrel and the optical joints between radiator and photon detector need also careful design. As shown below the design of the photon detector and its link to the radiator define the geometric dimensions of the latter.

3.4 Barrel Calorimeter

3.5 Forward Cherenkov

Two DIRC design options exist for the endcap part of the target spectrometer section. These differ in the photon readout design but both use an amorphous fused silica radiator disc. The endcap detector position covers forward angles of up to $\vartheta = 22°$ excluding an inner rectangular **(is it now elliptical??)** area of $\vartheta_x = 10°$ horizontal and $\vartheta_y = 5°$ vertical half-angles. Simulations using the DPM generator [4] give 1.0±0.8 (at 2 GeV/c) to 2.3±1.8 (at 15 GeV/c) charged particle multiplicity per $\bar{p}p$ interaction emitted from the target vertex into this acceptance.

In such a one-dimensional[1] DIRC type, a photon is transported to the edge of a circular disc while preserving the angle information. Avoiding too much light scattering loss at the surface reflections requires locally (in the order of millimeters) a surface roughness not exceeding several nanometers RMS.

The lower velocity threshold, which is common to both designs, depends on the onset of total internal reflection for a part of the photons emitted in the Cherenkov cone.

There are several boundary conditions for the disc thickness. Radiation length considerations as the detector is upstream of the endcap EMC call for a thin disc. The focussing design is workable with a 10mm thickness (X_0=126mm). Regarding the mechanical stability and handling during polishing, current company feedback recommends 20mm minimum thickness. The resulting thickness of the radiator disc has to be a compromise.

[1] Light is only reflected on surfaces of one spatial orientation, here the two disc surfaces both normal to the z axis.

3.5.1 Focussing Disc DIRC

In the Focussing Light guide Dispersion-Correcting design (Figures 5 and 6), when a photon arrives at the edge of the circular or polygonal disc, it enters into one of about hundred optical elements on the rim. Here the two-fold angular ambiguity (up-down) is lifted, the chromatic dispersion corrected and the photon focused onto a readout plane. While the optical element entered determines the ϕ coordinate, measuring the position in the dispersive direction on the focal plane of the focussing light guide yields the θ coordinate.

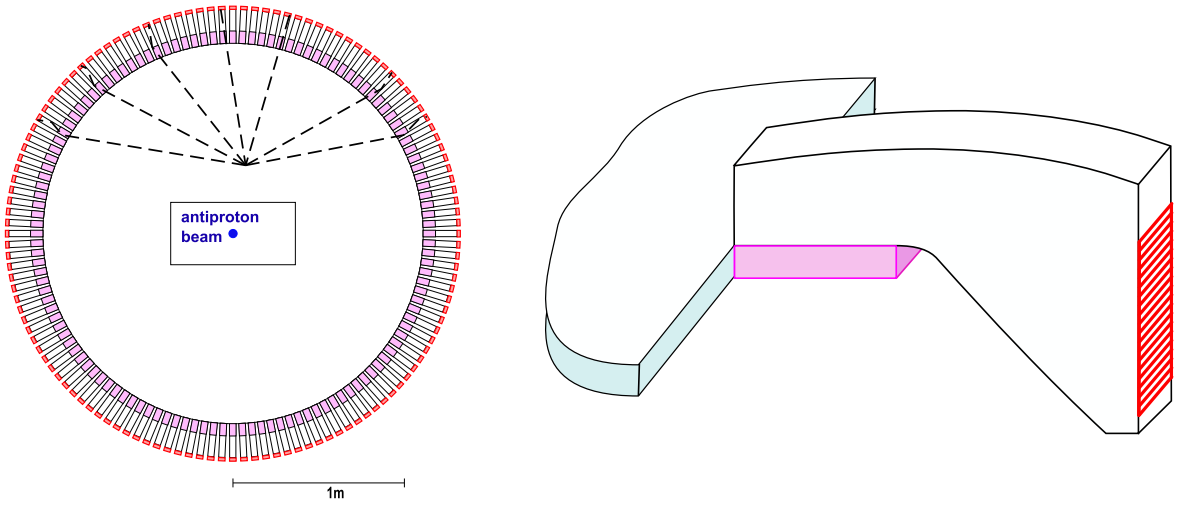

Figure 5: Polygonal disc with focussing light guides attached to the rim used as optical readout components.

Lithium fluoride (LiF) is UV transparent and has particularly low dispersion. Proton beam irradiation of a test sample shows that radiation-produced color centers are confined to sufficiently small wavelength ranges, and are only partially absorbing at the expected $\bar{\text{P}}$ANDA lifetime dose. Hence we believe we can use LiF as a prism element (see Fig. 6) to correct the Cherenkov radiation

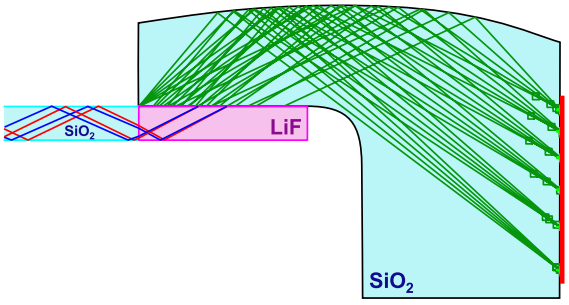

Figure 6: Light guide side view shown with a set of rays used for optimising the light guide curvature. Reflections at the parallel front and back surfaces keep the light inside but do not affect the focussing properties.

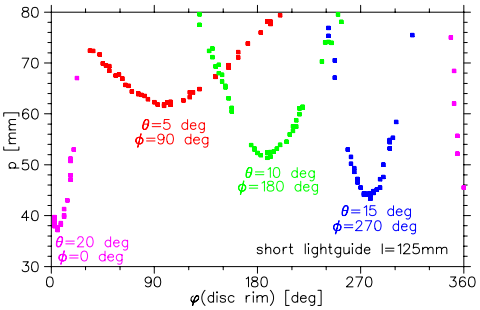

Figure 7: Simulated photon hit pattern for four particles emitted at different angles θ and ϕ from the target vertex.

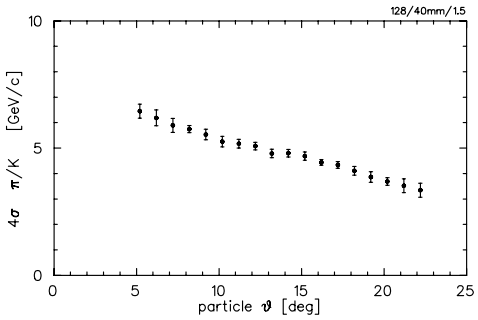

Figure 8: Simulation-derived pion-kaon separation power for a focussing lightguide design with a 15 mm thick amorphous fused silica disc and 0.4 eV photon detection efficiency. Calculation February 2008.

dispersion. The two boundary surfaces, with the radiator disc and the subsequent light guide, make the chromatic dispersion correction angle-independent to first order.

As with the radiator, the light impinging on the inside of the light guide's curved surface undergoes total internal reflection, hence no mirror coating is needed. This reflection makes the focussing also independent of the wavelength.

With the light staying within the dense optical material of the light guide, most of the incoming light phase space from the disc is mapped onto the focal plane with its one-coordinate readout. The focussing surface with cylindrical shape of varying curvature has been optimised to give an overall minimum for the focus spot sizes of the different angles on the focal plane, individual standard deviations being well below 1 mm for the instrumented area.

For an Endcap DIRC detector with 128 lightguides and 4096 detector pixels that fits inside the target spectrometer return yoke, Figure 8 shows the angle-dependent upper momentum limit being about 4–6 GeV/c for 4σ pion-kaon separation within the acceptance ϑ=5°–22°.

Typically all of the 40 detected photons per particle arrive within a 4 ns time window.

Each lightguide can individually be assigned its own 0.4 ns acceptance window. For the pixel size used in this simulation they are contained inside a 40 pixel·ns volume, which at 4K detector pixels amounts to 10 ps detector occupancy time per particle signature.

The detected photon rate (source: presentation KF 2007-03-27 Genova, 2E7 interactions; scaled to 4K pixels) is 3E7 s^{-1} per PMT and 1E6 s^{-1} per detector pixel.

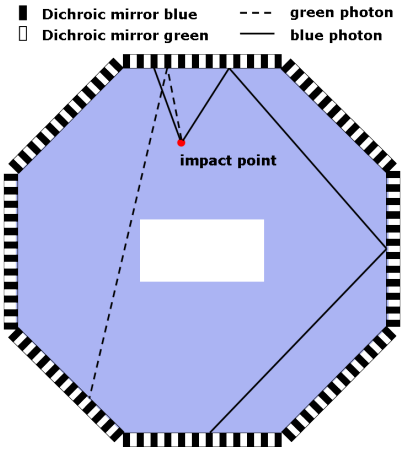

Figure 9: Sketch of the flightpath in the ToP Disc

3.5.2 Time of Propagation Disc DIRC

In the Multi-Chromatic Time-of-Propagation design ([5]) small detectors measure the arrival time of photons on the disc rim, requiring σ_t=30–50 ps single photon time resolution. For any given wavelength, the disc edge is effectively covered alternately with mirrors and detectors. Only due to the resulting different light path-lengths one can determine accurately enough the start reference time, i.e. the time when the initial charged particle enters the radiator, as the stored anti proton beam in the HESR has no suitable time structure to be used as an external time start.

As some of the light is reflected several times before hitting a detector, the longer path lengths allow a better relative time resolution.

The use of dicroic mirrors as color filters allows the use of multiple wavelength bands within the same radiator (the current design suggesting two bands) resulting in higher photon statistics. The narrow wavelength bands minimise the dispersion effects, and the quantum efficiency curve of the photo cathode material could be optimised for each wavelength band individually.

3.5.3 Proximity RICH

As alternative approaches Proximity Imaging Solutions were considered.

- Liquid radiator proximity RICH using CsI GEMs: Proximity focusing RICH detectors use the most simplest imaging geometry. Their resolution depends on the optical quality and crucially on the ratio of radiator thickness to stand-off distance, the distance between the creation and detection of the photon. Using liquid or solid radiators yielding enough Cherenkov photons, the radiator can be kept rather slim, which in turn only require moderate stand-off distances on the order of 100 mm. The ALICE HMPID detector is build in this fashion using a C6F14 liquid radiator and CsI-photon cathodes in an MWPC. This requires a UV optic. It is proposed to use the same radiator technique and combine the third tracking station with a CsI coated GEM photon detector. The detector will be thicker along the beam direction than the DIRC detector previously described, but can be essentially moved to any position along the beam axis. The estimated performance and the ALICE/STAR test results show a significant decrease in performance compared to the DIRC solutions.

- Solid radiator proximity RICH using CsI GEMs: One of the main drawbacks of using the ALICE design is the use of C6F14. This radiator is rather sensitive to impurities and radiation damage requiring a purification system. Using a fused silica disc with a properly machined surface as radiator circumvents the problem while keeping the geometrical advantages of the design. Initial studies show a further reduction of performance mainly due to strong dispersive effects in the UV region.

- Aerogel proximity RICH using PMTs: The Belle endcap Cherenkov threshold counter will be replaced by a proximity imaging RICH counter using an Aerogel radiator and conventional BiAlkali based multi-pixel PMTs as photon detectors. Using a so-called focusing radiator scheme, prototypes show excellent performances. The main technological challenge for this detector is to realise a photon detection matrix in a strong magnetic field. Recent developments in the field of proximity focusing HAPDs seem to make such a detector realistic. The large number of pixels required should the detector be placed behind the EMC, but inside the cryostat merit a detailed look at the costs of such a design.

3.5.4 Forward RICH

3.6 Forward Calorimeter

3.7 Muon Counter

The main purpose of the PANDA muon system is to achieve the highest efficiency in identification of muons in the medium-high energy range. Muons are present in the final state of many annihilation channels. Among them the physics program is mostly concentrated on dimuon production from Drell Yan at the maximum HESR momentum of 14.5 GeV/c or

J/ψ formation and decay in nuclear matter at 4.1 GeV/c momentum. In addition the study of rare decay of charmed particles could require a single muon identification. The most severe PID requirements to the muon system are set by the DY dimuon production, that has been selected as benchmark channel. Looser identification requirements are set by the J/ψ production channels, because of the strong kinematics constraint on the dimuon mass.

Due to the very low cross section ($\approx 1nb$) and to the unfavourable signal-to-noise ratio ($\approx 10^{-6}$) the maximum acceptance and efficiency are required. In the dimuon channels the simultaneous identification of a slow and of a fast muon is needed, with a strong correlation angle-momentum. Muon counters are foreseen both in the Target barrel part and endcap. In the Forward spectrometer the muon counters and filters will act as hadronic calorimeter. The azimuthal angle covered by the muon system ranges from 0^o to 120^o with a 2π polar angle coverage. With respect to the Letter of Intent the muon system has retained the original idea to use the solenoid yoke as muon filter. However the concept design has changed following the results of a preliminary acceptance study and the iron segmentation has been considered for the system optimization.
The momentum range of the DY muons reaching the barrel extends up to few GeV/c. The lower end of the range is fixed by the energy losses and the magnetic bending in the inner detectors (500 MeV/c).

The DY muons crossing the forward endcap show an energy range going from 1 to 3 GeV, with an average energy loss of 250 MeV before to enere the muon counters. The energy of the muons travelling through the Forward spectrometer can be greater than 10 GeV. *here relevant plots*
As a consequence slow muons, mainly produced in transverse direction cannot reach the muon system and must be identified by the inner detector. Medium and high energy muons are identified by the muon system only if they are positively detected by the muon detectors and properly match a charged primary track detected by the central tracker. The muon detector output that can be considered for identification purposes is the hit multiplicity in a selected region and, for isolated tracks, a momentum and direction measurement. Range measurement was also suggested as an effective tool for μ/π separation.

here relevant plots In this note preliminary results of the study of the layout for the muon system of the PANDA spectrometer are presented. With respect to the Letter of Intent the muon system has retained the original idea to use the magnet yokes as muon filter. However the concept design has changed following the results of a preliminary acceptance study and the iron segmentation has been considered for the system optimization.
Due to the impact on the solenoid project and to the time schedule for the magnet construction the optimization study of the muon system starts from the Target Spectrometer (TS), where the muon detectors should be alternatively inserted in sliced iron both in the barrel and the forward endcap.
The benchmark channel channel used for optimization is the Drell Yan production of muons pair

at 15 GeV/c.

3.7.1 TS simulation: generalities

The DY dimuon generation is based on a package written by A.Bianconi and described elsewhere (**??**). The generator is parametrized on experimental data at higher energies and extrapolated down to the PANDA energy range. (add details on scaling expected etc) A cut on dimuon mass at 1 GeV is applied by the generator to exclude the region where relevant background is expected from hadronic decays in lepton pairs([7]). However, the analysis three dimuon mass regions have been considered: the low mass LM one ($1.1 < IM(\mu\mu) < 1.5$),the medium mass MM ($1.5 < IM(\mu\mu), 2.5$) and the high mass one ($2.5 < IM(\mu\mu) < 5.5$). The MM region is considered almost free from hadronic decay contamination, whereas the HM region will contain the J/ψ decay. The LM region, even if partially affected by the hadronic contribution, is still considered in the simulation because of the statistical relevance of DY events in this region. The optimization of the muon system is based on the working hypothesis that the MM region will be the first choice for the physics analysis, as suggested in [**?**] due to the absence of contamination and the reasonable cross section.
The tracking of the particles through the experimental apparatus is based on the GEANT 4 package. Hit position, particle energy and direction both at the vertex and at the sensible layer are recorded. In the pion background simulation the position of the decay vertex, directions of parent and decay particle are also preserved.

The description of the apparatus geometry and of the materials crossed by the particles is based on the setup description given in the TDR ([**?**]). Whereas the barrel region is described in detail, in the endcap region of the TS only the forward EMC is considered for his relevance in terms of energy loss and hadronic interactions.

More refined simulation will be performed in preparation of the TPR using the simulation framework of the PANDA Collaboration still under development at the date of this study. In particular the design of the flux return iron in the TS is currently under discussion because of the mechanical problems due to the need to provide access and support for the inner detectors. In agreement with the suggestions from the Magnet Group a minimum width of 20 cm of non-segmented iron starting from the inner part of the yoke was considered in the simulation. Other constraints on the radial size of the yoke are also dictated by the maximum pipe length of the pellet target.

No muon detector description is introduced in the simulation. In order to study the possible segmentation configurations the positions of the muon detectors are represented by virtual sense layers in the iron. Number and radial position of the sense layers can be tuned to optimize the system configuration.

Additional virtual sense layers are added in radial direction at the entrance end at the exit of the detector volumes relevant for muon or hadron tracking.

3.7.2 TS simulation: layout description

here add infos on geometry considered, number of layers, drawing of the simulated setup, picture of the segmented iron as in last GS GSI presentation.

3.7.3 TS simulation: muon identification in the barrel

Muons are identified only if they are positively detected by the muon detectors. The muon detector output that can be considered for identification purposes is the hit multiplicity in a selected region and, for isolated tracks, a momentum and direction measurement. Range measurement was also suggested as an effective tool for μ/π separation.
The momentum range of the DY muons reaching the barrel extends up to few GeV/c. The lower end of the range is fixed by the energy losses and the magnetic bending in the inner detectors (500 MeV/c) and by energy loss and bending effects in the first part of the iron yoke (250 MeV/c). In the plot *here relevant plots*

4 Tools

In this section the TAG work is described. To evaluate the performance of the detectors the PID TAG defined the "Separation Power" as the right tool (see section **??**. With the help "Phase Space Plots" (section 4.2) the angular coverage and the coresponding particle momenta could be determined. The "Fast Simulation" (section 4.3) was used to map the separation power over the full angular and momentum range. In a second step important reactions and their relevant background channels were simulated. Thus the regions where a good separation power is needed could be identified and checked whether the detector performance is sufficient there.

4.1 Separation Power

This document completely deals with the quality of the particle identification of the projected PANDA detector. Thus the major issue upon which decisions can be made is a proper definition of classification quality or performance.

The according concept chosen for that purpose called 'Separation Power' bases on the assumption that the particular observables of objects of different classes exhibit more or less gaussian distributions.

Consider the situation illustrated in fig. 10.

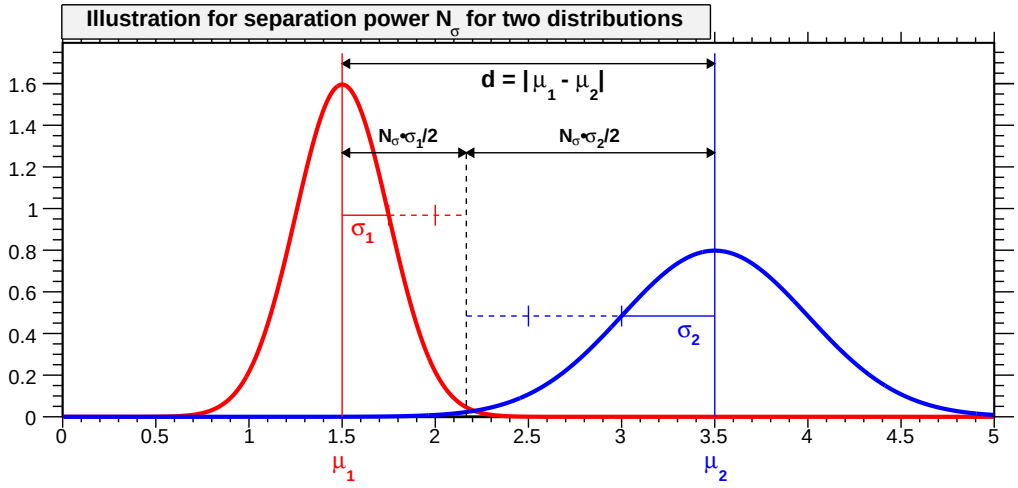

Figure 10: Illustration for the definition of separation power.

There are plotted two gaussian distributions $G_1(x) \equiv G(x; \mu_1, \sigma_1)$ and $G_2(x) \equiv G(x; \mu_2, \sigma_2)$ with mean values $\mu_1 = 1.5$ and $\mu_2 = 3.5$ and standard deviations $\sigma_1 = 0.25$ and $\sigma_2 = 0.5$. This could be e. g. the probability density distributions of the dE/dx measurements for two particle species in a small momentum range. Obviously the distributions are separable quite reasonable, but what is the measure for the separation potential?

A proper definition would be to define a particular classificator, e.g. every particle with property $x_0 < 2$ is considered as member of class 1 (red). Then one can determine two quantities which are of relevance for the qualtity of classification. The first one ist the efficiency, which is part of the distribution 1 (or a random sample of measurements following this distribution) which is identified correctly analytically corresponding to the integral

$$\epsilon = \int_{-\infty}^{x_0} G_1(x)\, dx \tag{2}$$

for a normalized Gaussian. The second quantity is the misidentification level given by the integral

$$\text{mis-id} = \int_{-\infty}^{x_0} G_2(x)\, dx \tag{3}$$

which is part of the distribution 2 in the same region thus identified incorrectly as being of class

1. These two values would define clearly the performance of the classificator[2]. But this solution cannot be applied in case when one does not want to define a particular selector. It rather has to be defined a measure for the prospective performance of a possible selector.

Exactly this is the aim of the separation power N_σ which relates the distance of the mean values $d = |\mu_1 - \mu_2|$ of the two distributions to their standard deviations σ_1 and σ_2. The usual unit of N_σ is 'number of gaussian sigmas of the separation potential', which is supposed to relate the number with gaussian integral values.

There are actually a lot of different definitions for that quantity on the market but it has been found an agreement within the PID TAG on the following definition:

$$N_\sigma = \frac{|m_1 - m_2|}{\sigma_\beta} = \frac{|m_1 - m_2|}{(\sigma_1/2 + \sigma_2/2)} \tag{4}$$

This relationship is illustrated in fig. 10. The black dashed line marks the position x_0 between the two distributions, for which the differences to each mean value $|m_1 - x_0| = N_\sigma \cdot \sigma_1/2$ and $|m_2 - x_0| = N_\sigma \cdot \sigma_2/2$ are the same in terms of σ's.

This means a separation of e. g. $N_\sigma = 4\sigma$ corresponds to a gaussian integral

$$I = \int_{-\infty}^{\mu+4\sigma/2} G(x;\mu,\sigma)\,dx = 0.9772 \tag{5}$$

which shall express an efficiency around $\epsilon \approx 97.7\%$ or a mis-ID level around mis$=100\% - 97.7\% \approx 2.3\%$ or both. This integration up to half the number of sigmas $N_\sigma/2$ seems a bit contra intuitive but is common notion and therefore has kept for the considerations in this document. Another feature of this definition is that it is symmetric for both classes or distributions, even with different σ's. Furthermore for the particular case of normalized gaussian distributions and a selector requiring $x < x_0$ for classifying class 1 objects in the upper example, the efficiency ϵ and purity π for this selection have the same value, since

$$\epsilon = \frac{\int_{-\infty}^{x_0} G_1(x)\,dx}{\int_{-\infty}^{+\infty} G_1(x)\,dx} = \frac{\int_{-\infty}^{x_0} G_1(x)\,dx}{1} = \frac{\int_{-\infty}^{x_0} G_1(x)\,dx}{\int_{-\infty}^{x_0} G_1(x)\,dx + \int_{x_0}^{+\infty} G_1(x)\,dx} \tag{6}$$

$$= \frac{\int_{-\infty}^{x_0} G_1(x)\,dx}{\int_{-\infty}^{x_0} G_1(x)\,dx + \int_{-\infty}^{x_0} G_2(x)\,dx} = \frac{\int_{-\infty}^{x_0} G_1(x)\,dx}{\int_{-\infty}^{x_0} G_1(x) + G_2(x)\,dx} = \pi \tag{7}$$

Tab. 2 lists on the left hand side the mis-id levels $1 - \int G(x)dx$ with 1-sided and 2-sided gaussian integrals for different values of N_σ, on the right hand side the corresponding values of the separation power for given levels of mis-id according to the upper definition. It shall be emphasized again that for given values N_σ the integration is only performed up to $N_\sigma/2$, therefore the mis-id levels might seem surprisingly high for given number of σ's separation.

Taking into account that quantities in reality never have gaussian shape the values σ in fact are not necessarily gaussian sigmas but calculated as the root-mean-square (which actually is the standard deviation)

$$\sigma_{\mathrm{rms}} = \sqrt{\sum_i (x_i - \mu)^2} \tag{8}$$

[2]For Bayes' classification a flux correction would have to be taken into account additionally. This requires of course knowledge about a posteriori probabilities of particle fluxes which not necessarily is available since significantly dependent on the given trigger and reaction type.

what in case of gaussian distribution would be indeed identical with the gaussian σ from above. For the given example in fig. 10 the definition (4) computes to

$$N_{\sigma,1} = \frac{2}{0.25/2 + 0.5/2}\,\sigma = \frac{2}{0.375}\,\sigma = 5.333\,\sigma \quad .$$

Another issue with directly is connected with the upper definition is the question how to define the combined separation $N_{\sigma,\mathrm{tot}}$ e.g. for values $N_{\sigma,i}$ achieved by various detector components to express the overall performance. The agreement of the PID-TAG concerning this was to consider the quadratic sum

$$N_{\sigma,\mathrm{tot}} := \left(\sum_i N_{\sigma,i}^2\right)^{1/2} \tag{9}$$

as a good measure. In order to evaluate the goodness of that expression it first of all is necessary to make aware what meaning the value N_σ has in terms of probablity. When considering something similar to equation (5) as a appropriate measure, namely the integral of a Gaussian from $-N_\sigma/2$ to $+N_\sigma/2$ the expression for the corresponding probability of mis-identification is given by

$$P_{\mathrm{mis}}(N_\sigma) = 1 - \int_{-N_\sigma/2}^{+N_\sigma/2} G(x;\mu=0,\sigma=1)\,dx \tag{10}$$

which directly defines the mis-identification probability for n statistically independent separation capabilities as the product

$$P_{\mathrm{mis,tot}} = P_{\mathrm{mis}}(N_{\sigma,1}) \times \cdots \times P_{\mathrm{mis}}(N_{\sigma,n}) \tag{11}$$

in addition. Hence equation (10) implicitly specifies $N_{\sigma,\mathrm{tot}}$ as that value where the intergral yields exactly $P_{\mathrm{mis,tot}}$. This procedure has been pursued for two values $N_{\sigma,1}$ and $N_{\sigma,2}$ as presented in fig. 11. In (a) the combined separation power is shown as 2-dimensional function of the two input values, (b) presents the difference

$$\Delta = \left| N_{\sigma,\mathrm{tot}} - \sqrt{N_{\sigma,1}^2 + N_{\sigma,2}^2} \right| \tag{12}$$

of the resulting value and equation (9), which obviously reasonably reproduces the correct value with a maximum deviation of about 0.5σ in the range of single values up to $N_\sigma = 6$.

4.1.1 Parametrization of the Electromagentic Calorimeter

Although not implemented in the Fast Simulation, a parametrization of part of the response of the EMC has been persued for the estimation of overall PID quality. It is based on fully simulated data but only information about electron-pion-separation was taken into account up to now. Fig. 12 (a) shows the distributions of the parametrized ratio of the calibrated cluster energy in the electromagnetic calorimeter and the reconstructed track momentum E_{clus}/p for simulated electrons (green) and pions (black). The source for modelling the parametrizations can be found in the PANDA Physics Book [**?**]. It is clearly visible that above momenta of approximately 500 MeV this quantity is a powerful tool to separate electrons from pions, demonstrated in fig.12 (b), where the separation power has been determined dependend of the track momentum p by the

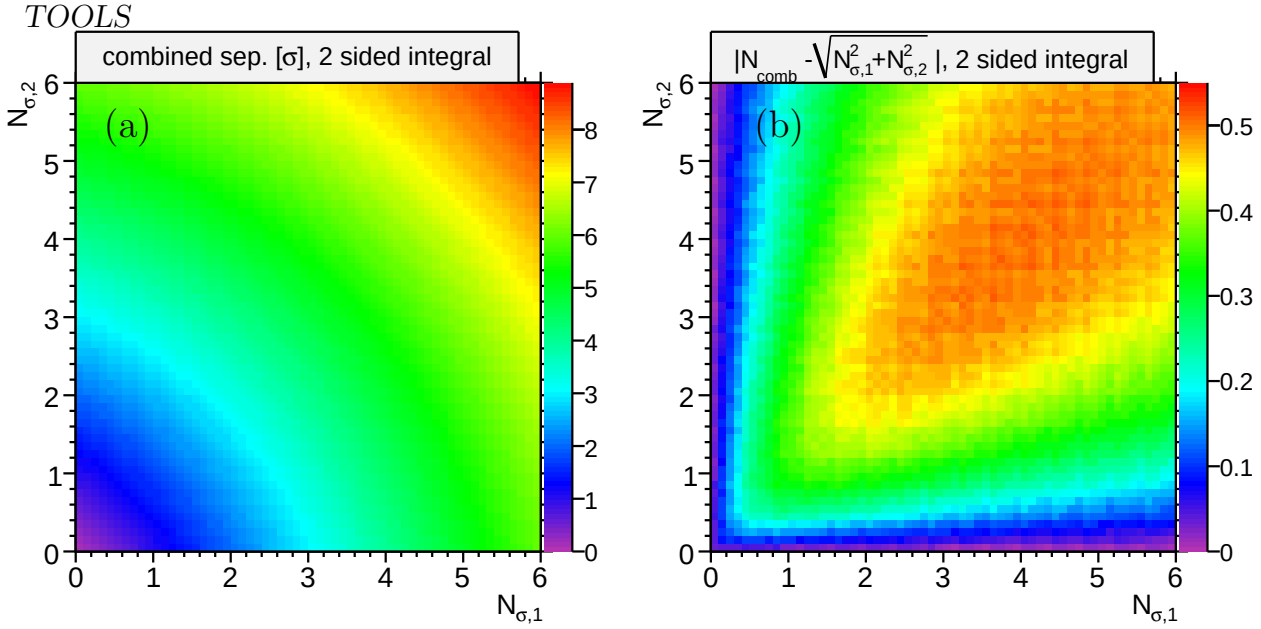

Figure 11: (a) Graphical representation of the combined separation power $N_{\sigma,\mathrm{tot}}$ of two values $N_{\sigma,1}$ and $N_{\sigma,2}$, (b) the corresponding difference $\left|N_{\sigma,\mathrm{tot}} - \sqrt{N_{\sigma,1}^2 + N_{\sigma,2}^2}\right|$.

N_σ	mis-id (1s) [%]	mis-id (2s) [%]	mis-id [%]	N_σ (1s)	N_σ (2s)
1.0	30.854	61.708	10.000	2.6	3.3
2.0	15.769	31.538	5.000	3.3	3.9
3.0	6.681	13.361	1.000	4.6	5.1
4.0	2.254	4.507	0.500	5.1	5.6
5.0	0.621	1.242	0.100	6.2	6.6
6.0	0.133	0.266	0.050	6.6	7.0
7.0	0.023	0.047	0.010	7.4	7.8
8.0	0.003	0.006	0.005	7.8	8.1
9.0	0.000	0.001	0.001	8.5	8.8

Table 2: Relation between separation power and mis-id level

definitions given above. Since no θ dependence was available this separation power is assumed to be constant over the complete θ range.

According to the software chapter of the PANDA Physics Book e/π separation is the most difficult one. Therefore this distribution is assumed to also hold for separating electrons from any other particle species.

As a very naive assumption without a proof the additional separation power provided by the EMC for any other particle combination is taken to be 1σ over the complete phase space covered by the EMC.

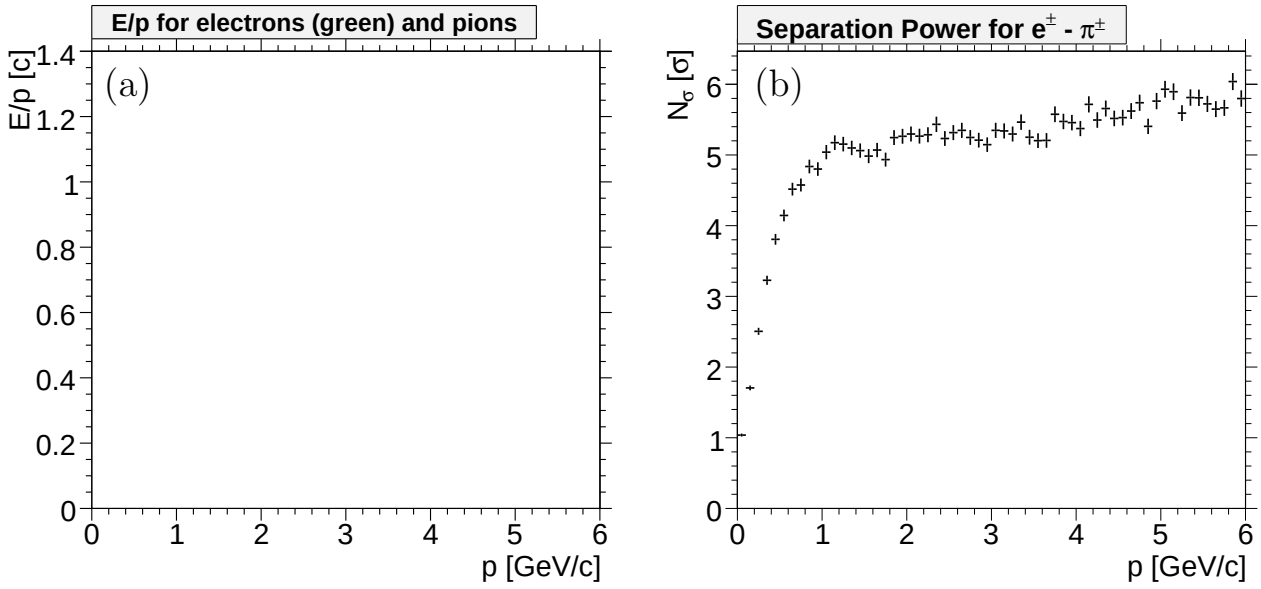

Figure 12: (a) Parameterized distribution of E_{clus}/p for electrons and pions and (b) the resulting separation power N_σ as function of the track momentum p.

4.1.2 Mapping Separation Power

For the purpose of illustration the relationship between kinematic distributions of physics channels and the PID quality the separation power defined in (4) has been determined as 2-dimensional histogram in phase space (p, θ). Therefore it was necessary to computed the mean value μ and standard deviation σ for every bin i with $[p_i \ldots p_i + dp; \theta_i \ldots \theta_i + d\theta]$ for bin widths dp and $d\theta$ for every detector and particle species.

One technical remark: To avoid the computation of $(x - \mu)$ for every measurement in order to determine σ, which is very time consuming for large datasets, the relationship

$$\sigma = \frac{1}{N}\sqrt{\sum x_i^2 - \left(\sum x_i\right)^2} \tag{13}$$

has been exploited which does not require a previous calculation of the mean value $\mu = \bar{x}$.

In order to evaluate the contributions of the various detectors to the overall classification potential, the separation power defined above has been determined for every single detector component and all possible particle combinations, which add up to the following 10 possibilies:

1. $e^\pm - \mu^\pm$, $e^\pm - \pi^\pm$, $e^\pm - K^\pm$, $e^\pm - p/\bar{p}$,
2. $\mu^\pm - \pi^\pm$, $\mu^\pm - K^\pm$, $\mu^\pm - p/\bar{p}$,
3. $\pi^\pm - K^\pm$, $\pi^\pm - p/\bar{p}$,
4. $K^\pm - p/\bar{p}$.

The results are determined based upon 5 million isotropic distributed single track events with particle momenta up to 6 GeV/c.

Figs. 13 and 14 shows as an example the p–θ–dependent power for electron–kaon separation for all 8 detector components

- Micro Vertex Detector (MVD)
- Barrel Time of Flight System (TOF)
- Barrel DIRC
- Disc DIRC
- Ring Image Cherenkov Detector (RICH)
- Electro Magnetic Calorimeter (EMC)
- Straw Tube Tracker (STT)
- Time Projection Chamber (TPC)

under investigation. The color codes in these 2 dimensional representations correspond to the numbers of σ's N_σ of separation with a cutoff $N_\sigma > 8$, so in the red regions are possibly values above that limit.

To get an impression of the overall particle identification performance the values $N_{\sigma,i}$ from the different detectors i have been combined by quadratic summation according to (9) under the assumption of statistically uncorrelated $N_{\sigma,i}$. Since there are two central tacker options (STT and TPC) which cannot contribute to the same total separation, two different scenarios with either the STT or the TPC are considered separately. Fig. 15 shows the combined information for the STT option and fig. 16 for the detector setup with the TPC as central tracker. All maps are based on the requirement of positiv identification of a particle species. This means, that particle type A is only considered to be dsitinguishable from another particle type B when both create a signal in the particular detector and the given phase space region.

One should keep in mind that the conclusive power of separations involving electrons and muons is limited for the time being since only limited information from the electromagnetic calorimeters and none for the muon detectors has been incorporated so far, which has significant impact on electron and muon identification respectively.

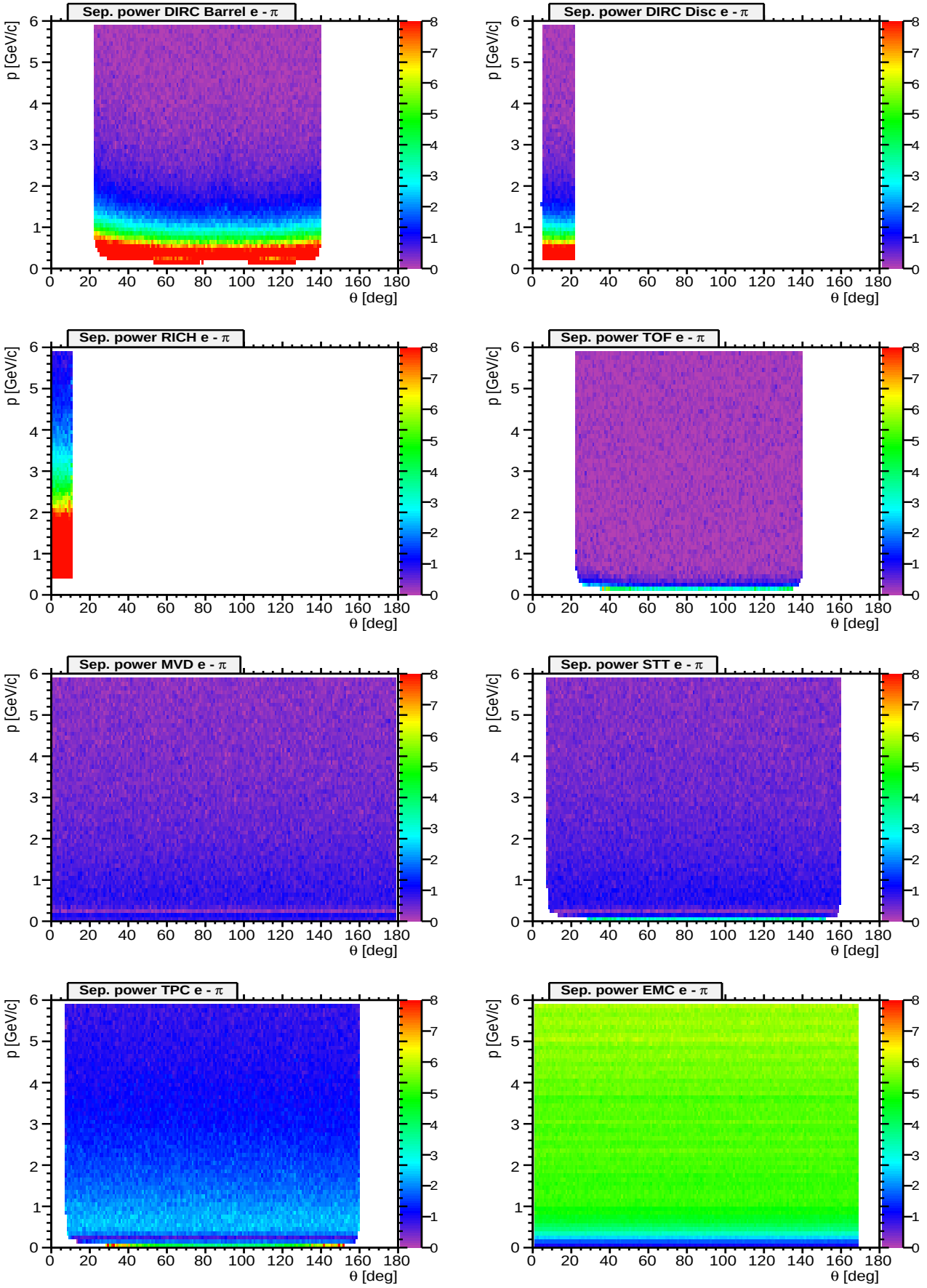

Figure 13: Map of separation power for $e^{\pm}$–$\pi^{\pm}$ separation. Color code corresponds to $N_\sigma = 0 \ldots 8$.

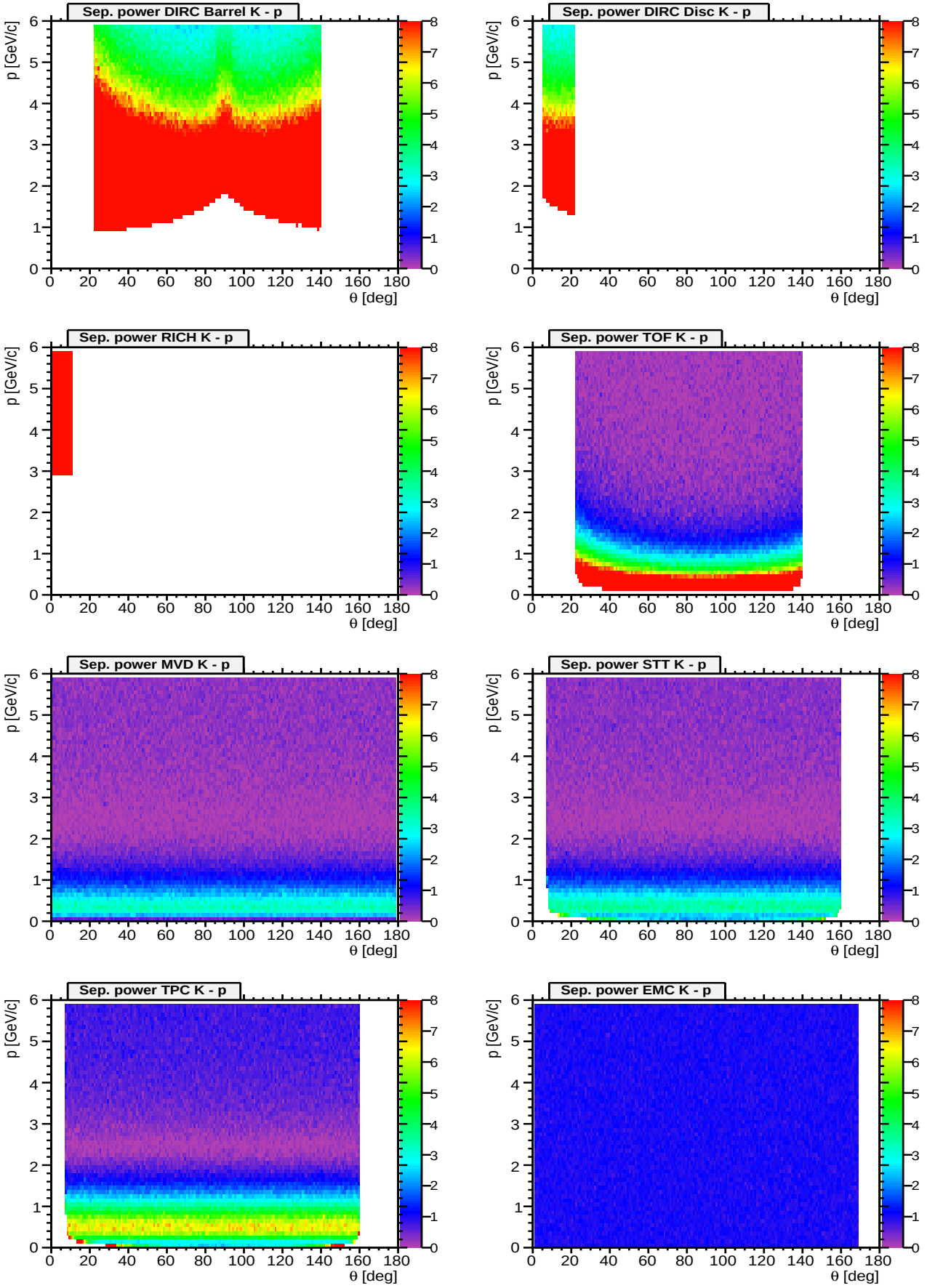

Figure 14: Map of separation power for $K^{\pm}$–$p/\bar{p}$ separation. Color code corresponds to $N_\sigma = 0 \ldots 8$.

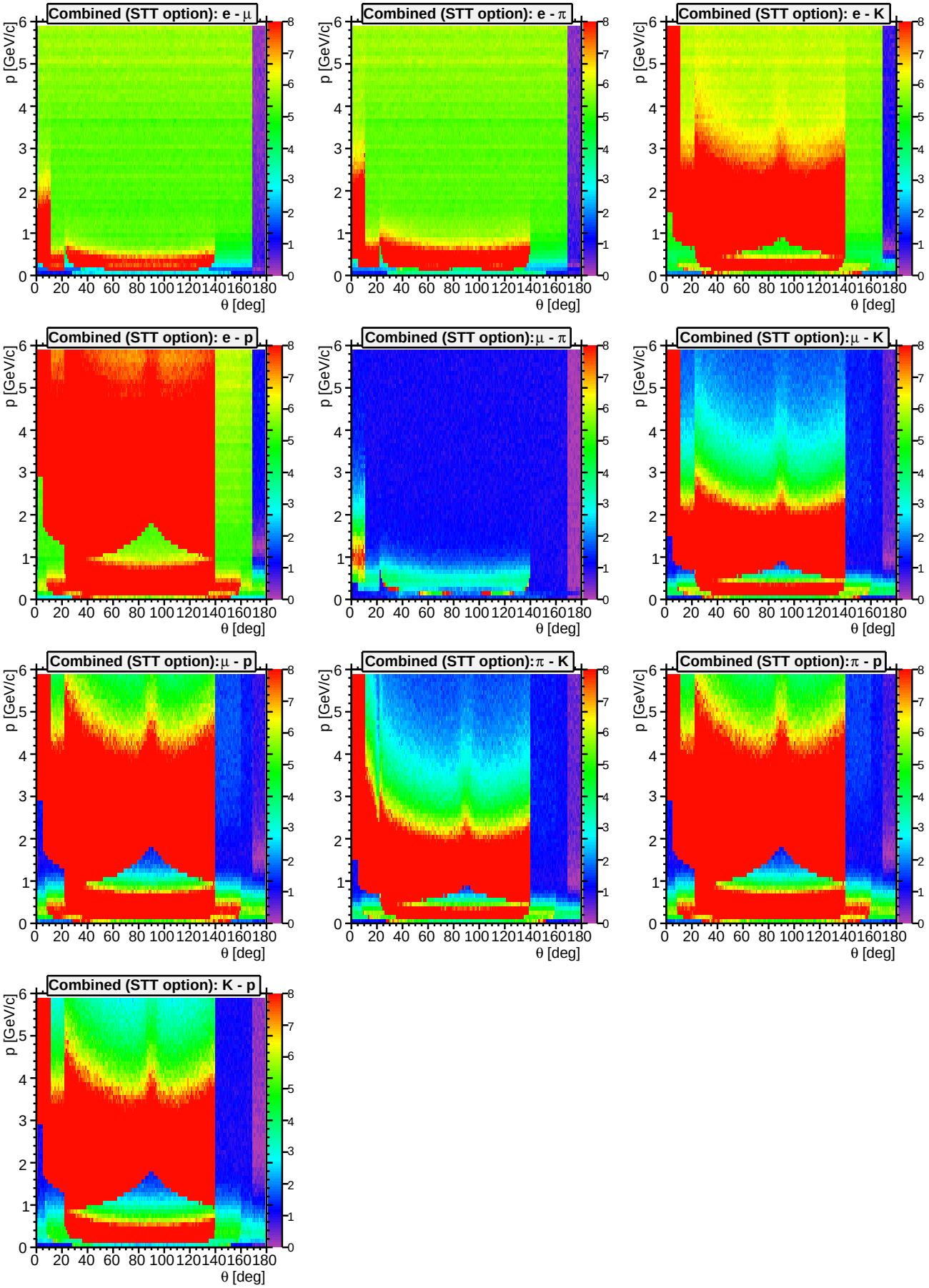

Figure 15: Combined map of Separation Power with STT as central tracker option. Color code corresponds to $N_\sigma = 0 \ldots 8$.

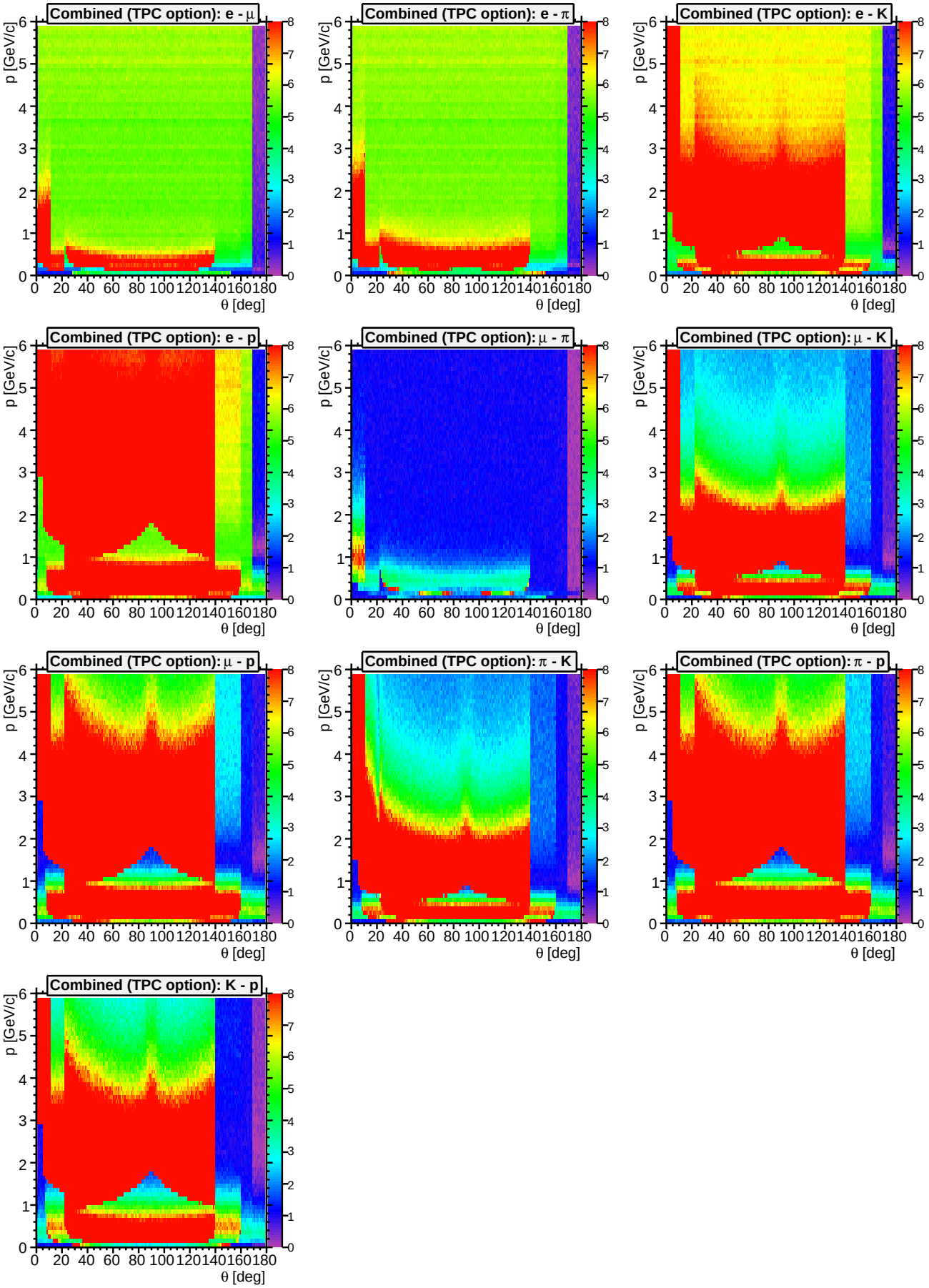

Figure 16: Combined map of Separation Power with TPC as central tracker option. Color code corresponds to $N_\sigma = 0 \ldots 8$.

4.2 Phase Space Plots

The question which has to be answered concerning particle identification is not only how good the classification works or has to work, but also in which region of the phase space one needs good separation, and in which parts one possibly doesn't need almost any.

Therefore it is a crucial task to visualize the kinematic behaviour of various important physics channels to get a better insight to the above issue. Furthermore not only kinematic distributions of signal events are relevant, since good PID is only useful in cases where kinematic overlap of particles of species A from signal events and particles of species B from background events really exists. In scenarios where particles of the same type A appear in signal as well as background events in the same phase space location the background suppression cannot be improved by means of PID.

Following a request of the PID TAG phase space plots from all the reactions relevant for the physics book were produced. The set of plots shows for each particle species of the reaction the particle momentum versus theta angle.

Tab. 4 lists part of the benchmark channels discussed in the PANDA Physics Booklet and some additional ones to study inclusive open charm analysis together with relevant background channels. In particular channels were investigated which might suffer significantly from insufficient PID capabilities[3].

The acronym DPM in the table refers to generic background evens generated with the **D**ual **P**arton **M**odel generator. In the last column references to the corresponding figures are given. Tab. 3 gives some standard decay channels which apply to cases where nothing different is specified in tab. 4.

In figs. 17 - 21 kinematic distributions (momentum p vs. dip angle θ) at various beam momenta are shown for some of the signal-background scenarios listed in 4, one particle species per plot. To easier spot signal and background, the latter ones are colored blue.

Particle	Decay channel
J/ψ	50% e^+e^-, 50% $\mu^+\mu^-$
η	$\pi^+\pi^-\pi^0$
D^0	$K^-\pi^+$
D^+	$K^-\pi^+\pi^+$
D^{*+}	50% $D^0\pi^+$,50% $D^+\pi^0$
D^{*0}	$D^0\pi^0$
D_s^+	$\phi\pi^+$
ϕ	K^+K^-
Λ	$p\pi^-$
π^0	$\gamma\gamma$

Table 3: Standard decay channels for some particles

[3]Signal channels with background reactions comprising the same final state can only be identified due to different kinematic behaviour, which goes beyond the capabilities of PID

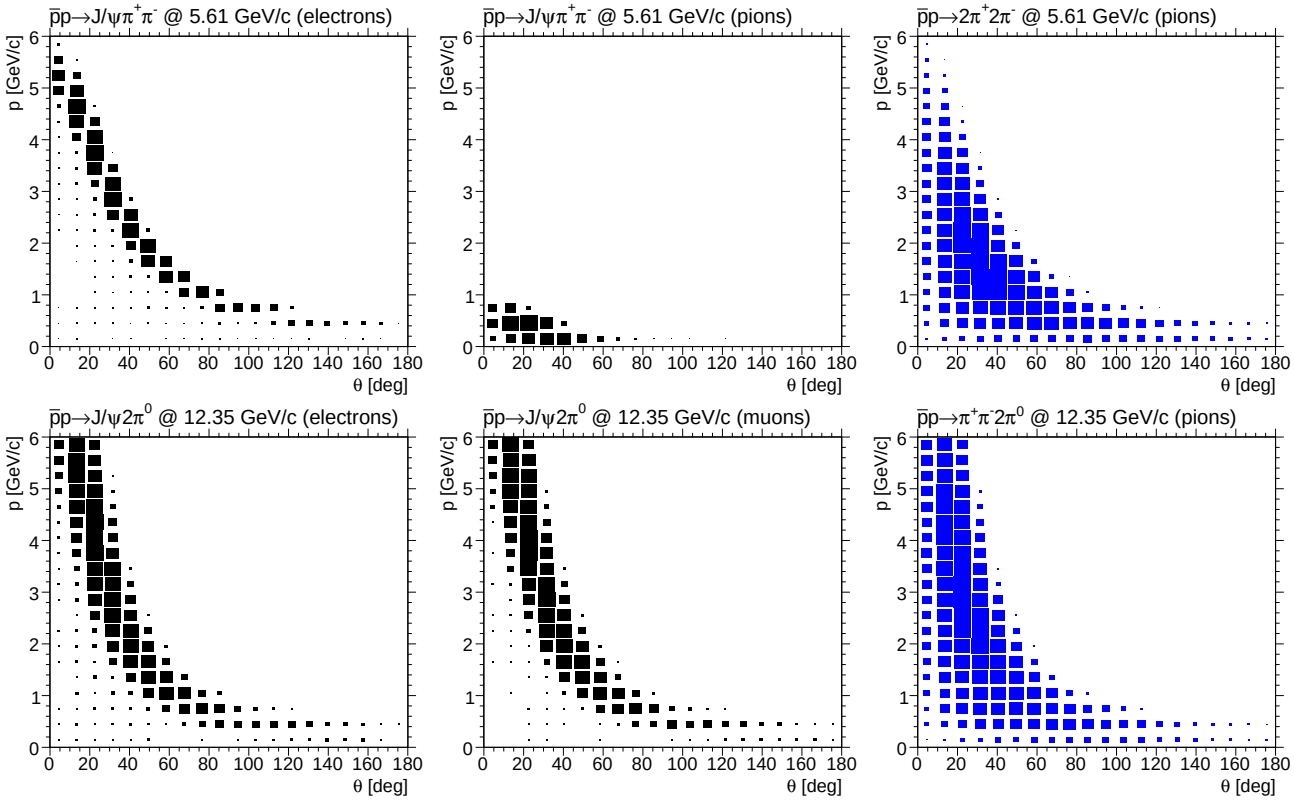

Figure 17: $\bar{p}p \to J/\psi\pi^+\pi^-$ @ 5.609 GeV/c (top), $\bar{p}p \to J/\psi 2\pi^0$ @ 12.3485 GeV/c (bottom)

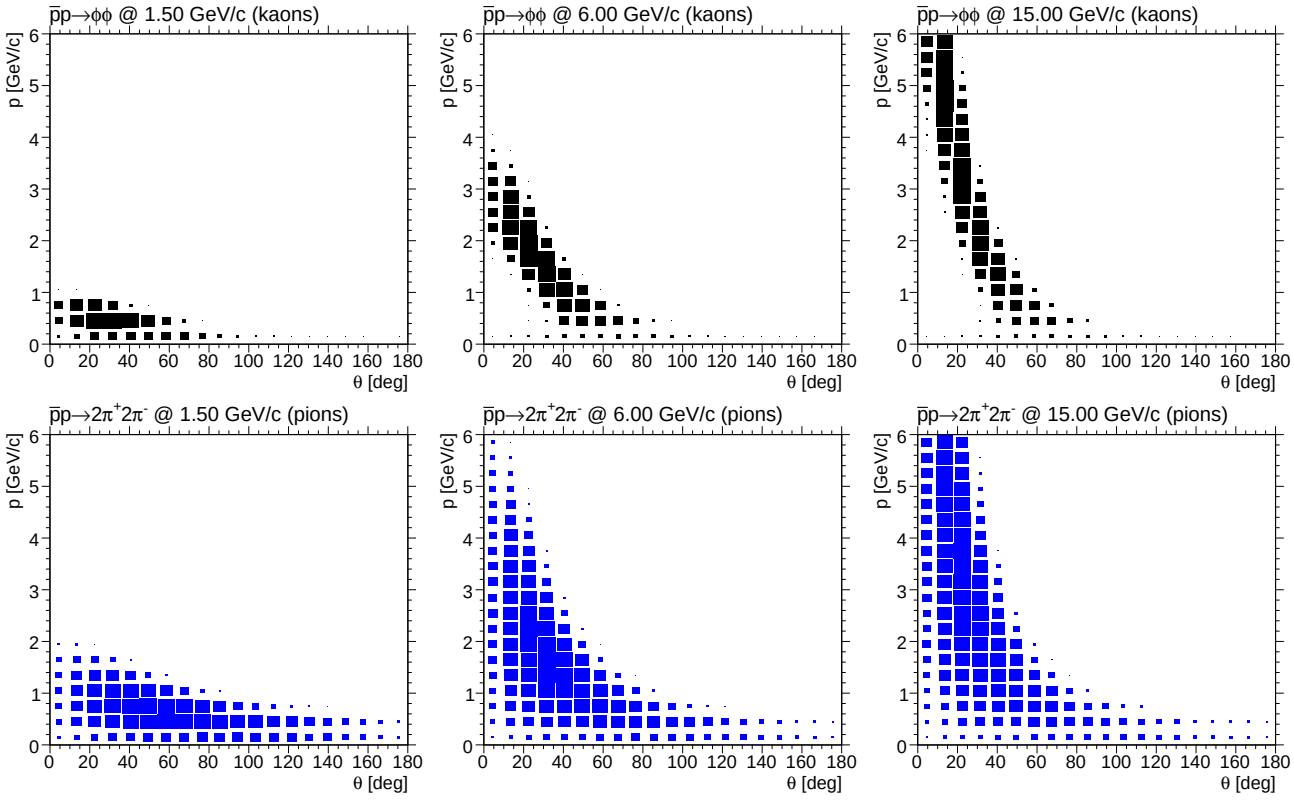

Figure 18: $\bar{p}p \to \phi\phi$ @ 1.5, 6.0, 15.0 GeV/c

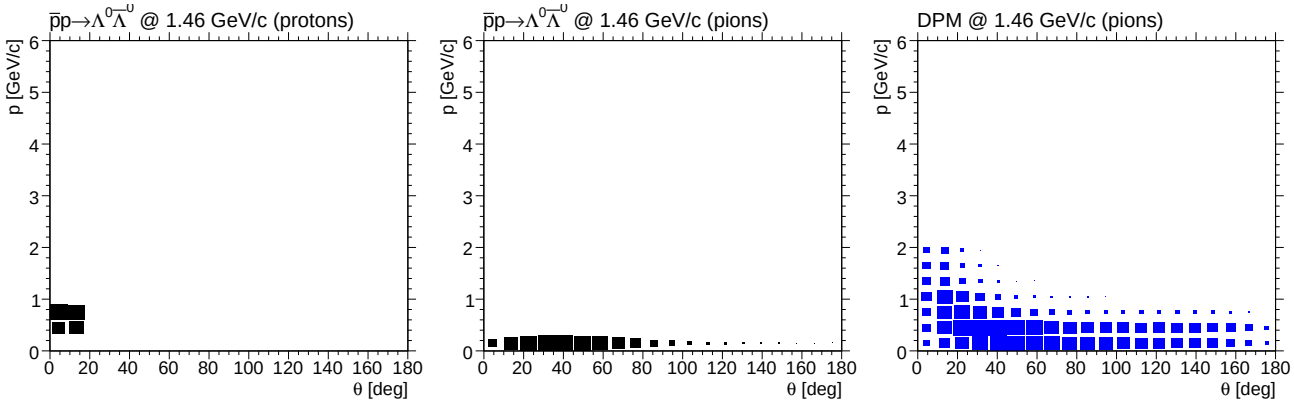

Figure 19: $\bar{p}p \to \Lambda^0\bar{\Lambda}^0$ @ 1.4601 GeV/c

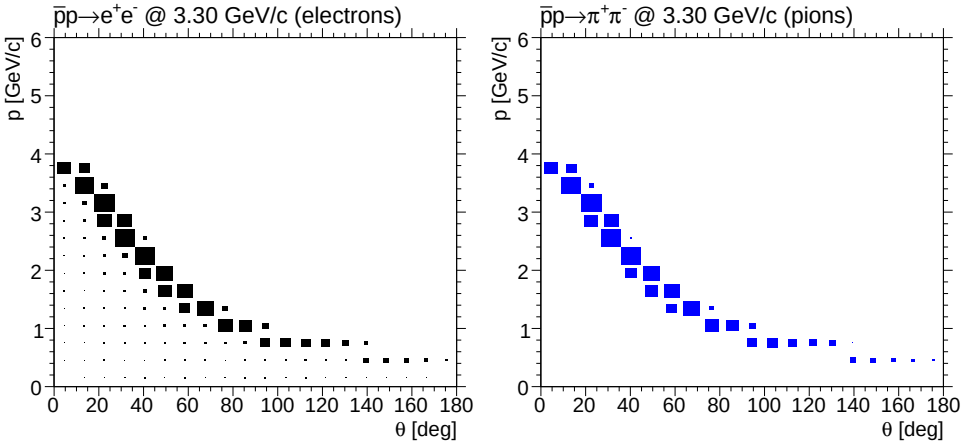

Figure 20: $\bar{p}p \to e^+e^-$ @ 3.30 GeV/c

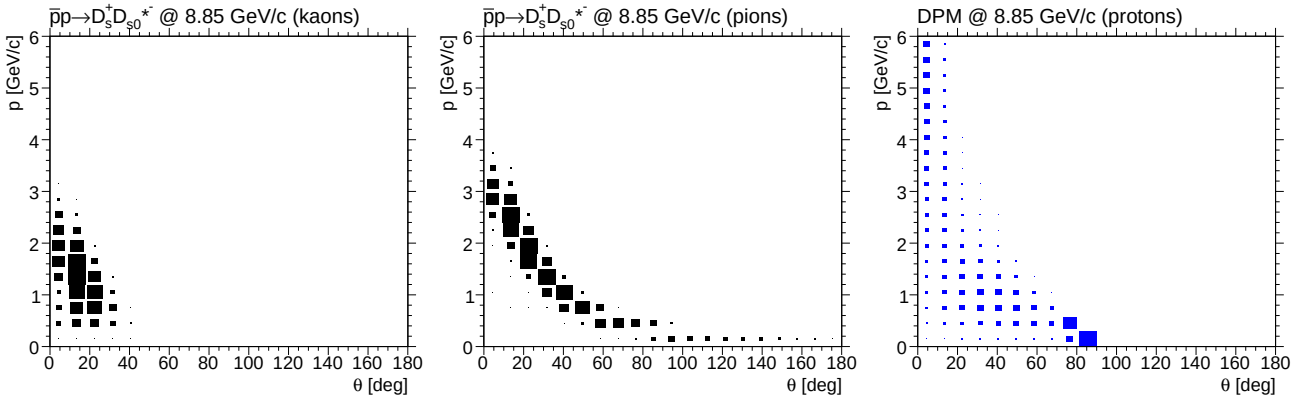

Figure 21: $\bar{p}p \to D_s^+ D_{s0}^*(2317)^-$ @ 8.847 GeV/c

Signal	**Background**	$\boldsymbol{p_{\bar{p}}}$ **[GeV/**$\boldsymbol{c}$**]**	**Fig.**
$J/\psi 2\pi^0$	$\pi^+\pi^- 2\pi^0$	5.609 / 6.232 /8.682	
		10.295 / 12.349	17
$J/\psi\pi^+\pi^-$	$2\pi^+2\pi^-$	5.609 / 6.232 / 6.988	
		8.682 / 10.295 / 12.349	-
	$2\pi^+2\pi^-\pi^0$	6.990 / 8.7	-
$J/\psi\eta$	$2\pi^+2\pi^-$	6.080 / 6.990 / 8.7	-
	$3\pi^+3\pi^-$	6.080 / 6.990 / 8.7	-
$\phi\phi$	$2\pi^+2\pi^-$	1.5 / 6.0 / 12.0 / 15.0	18
	$3\pi^+3\pi^-$	1.5 / 6.0 / 12.0 / 15.0	-
$\Lambda^0\bar{\Lambda}^0$	$\Sigma^0\bar{\Sigma}^0$	1.914 / 3.101 / 6.0	19
	DPM	1.460 / 8.0 / 10.0	-
e^+e^-	$\pi^+\pi^-$	1.7 / 3.3 / 7.9 / 10.9 / 15.0	20
$D_s^+ D_{s0}^*(2317)^-$	DPM	8.847	21
	$3\pi^+3\pi^-\pi^0$	8.847	-
$D_s^+ D_s^-\gamma$	$3\pi^+3\pi^-$	8.847	-
	DPM	7.361 / 7.746 / 8.0 / 12.0 / 15.0	-
$D^{*0}\bar{D}^{*0}\gamma$	DPM	7.746 / 8.0 / 12.0 / 15.0	-
$D^{*+}D^{*-}\gamma$	DPM	7.746 / 8.0 / 12.0 / 15.0	-
$D^0\bar{D}^0\gamma$	DPM	6.488 / 8.0 / 12.0 / 15.0	-
$D^+D^-\gamma$	DPM	6.488 / 8.0 / 12.0 / 15.0	-

Table 4: Table of Phase Space Channels

4.3 Fast Simulation

In order to get information about phase space (i.e. momentum-polar angle dependence) coverage of the different PID relevant subsystems maps of separation power have been generated based on fast simulations of single track events, i.e. the particles properties are modified with an effective parametrization of detectors responses and PID information is estimated and attached to the resulting particle candidate. Since no microscopic simulation is performed and no exact geometry information is taken into account, the accuracy of this approach is limited, the computation time on the other hand is orders of magnitude shorter offering the possibility to do studies with higher statistics.

4.4 General Technique

In contrast to microscopic simulations using software systems like Geant or Fluka the Fast Simulation is based on acceptance filtering and effective parametrization of all observables of the particular subsystems. Underlying assumption is that the detector system will be able to recontruct the true particles properties like momentum, direction, energy, charge and particle identification (PID) information with uncertainties which are basically uncorrelated and can be described reasonable by parametric models. That could as simple example be gaussian uncertainty for momentum reconstruction with $\delta p/p = \sigma_p = 2\%$, which will be used to modify the true (i.e. generated) tracks parameters accordingly. Additionally a simple geometric accptance requirement will decide whether a track has been detected by a particular detector component or not.

There is a lot of freedom for the implementation of the subsystems, but a minimalistic detector description comprises

- Sensitivity information: Detects charged or neutral particles or both?
- Polar angle coverage: $\theta_{\min} < \theta < \theta_{\min}$
- Gaussian resolution of observables: $\sigma_1, \ldots, \sigma_n$

In order to apply these simulation scheme for every trackable particle coming from the event generator the following procedure is processed:

1. For all detectors D_j, $1 < j < m$
   - In case D_j detects the particle, collect resolution information for all measurable quantities.
2. When no detector detected the track, skip it.
3. Merge all resolution information; when e. g. the particle has been detected by n devices capable of measuring momentum p with resolutions $\sigma_{p,1}, \ldots, \sigma_{p,n}$, the total resolution is

$$\sigma_p = \left(\sum_{i=0}^{n} \frac{1}{\sigma_{p,i}^2} \right)^{-\frac{1}{2}}$$

4. Modify the according quantities x of the original track in the way $x' = x + \delta x$, with δx randomly chosen from gaussian distribution $G(\mu = 0, \sigma_x)$

5. Create PID information according to the particles properties and attach to the particle; add particle to the track list

6. (Optional) Create secondary particles related to particles properties and add to the track list

With the so prepared track list analysis can be performed. The interface for doing that is exactly the same as the one for full simulated events.

Since this document is focussing on PID the relevant features will be describe in more detail in the following chapters. This will be done effect– or observable–wise instead of detector–wise, since the observed quantities

- specific energy loss dE/dx (MVD, TPC, STT)
- Cherenkov angle θ_C (Barrel DIRC, Disc DIRC, RICH)
- reconstructed squared mass m^2 (TOF)
- EMC related measurements like E_{cluster}/p or Zernike momenta
- signals from Muon Chambers

govern the PID quality and performance and thus are a better ordering criterion. Unfortunately the latter two informations from e.-m. calorimetry and the muon detectors are not implemented in the Fast Simulation for the time being.

4.5 Tracking Detectors

Although not of direct impact to the field of PID the process of tracking delivers vital information for many of the PID relevant systems. Most of these like e.g. the Time-of-flight (TOF) system or Cherenkov devices (DIRCs and RICH) do not allow for performing a stand alone position measurement, thus their information have to be linked to tracks reconstructed by tracking devices. In addition for the purpose of evaluating PID likelihood functions one usually needs to compute expected values for observables like the Cherenkov angle θ_C or energy loss dE/dx which will be computed for the reconstructed momentum value of the track. This certainly will differ from the true momentum value and therefore track reconstruction accuracy has important impact on likelihood based classification methods.

The approach for reconstruction of momenta in the Fast Simulation nevertheless is a very simple one assuming a global momentum resolution $\delta p/p$ for the track reconstruction, since due to technical reasons the particular detector components cannot exchange information. This implies that the tracking devices are not able to feed their information into the PID systems.

4.6 Energy Loss Parametrization

The computation of the specific energy loss is based on the Bethe-Bloch formula which very precisely takes into account the processes of charged particles interacting with matter. The formula and detailled information about parameter meanings in this term can be found in [6].

The expression looks quite complicated but can be evaluated straight forward with momentum p and mass m given as input. Additionally one has to substitude a lot of other, material related constants. Since we are not interested in the absolut energy loss but only in relative losses for different particle species it is not crucial to have very precise knowledge about the fixed parameters.

In order to generate a simulated detector response for detectors capable of measuring dE/dx a gaussian resolution $\sigma_{dE/dx}$ has been set for each of them. The simulated measured $(dE/dx)_{\text{sim}}$ value thus has been simply computed with formula (**??**) to

$$\left(\frac{dE}{dx}\right)_{\text{sim}} = \left(\frac{dE}{dx}\right) + \delta\left(\frac{dE}{dx}\right) \tag{14}$$

with randomly chosen value $\delta(dE/dx)$ from a gaussian distribution $G(\mu = 0, \sigma_{dE/dx})$.

4.7 Cherenkov Angle Parametrization

Basic theoretical information about the origin of Cherenkov radiation can be found elsewhere and will not be discuss here. The Cherenkov angle defined as the opening angle of the cone of radiation relativ to the direction of the incident charged particles momenta in medium with refractive index n is given by the expression

$$\theta_C = \arccos\left(\frac{1}{\beta \cdot n}\right) \tag{15}$$

with $\beta = p \cdot c/E$ being the velocity of the particle. Obviously computation of the expected Cherenkov angle for any given particle detected by the specific detector is straight forward. Key ingredient of the parametrization of the detector response is the resolution estimation. In case of DIRC detectors experience from the working device in the BaBar experiment tells us that the overall reconstruction resolution of the Cherenkov angle can be based on a single photon resolution $\sigma_{\text{s.phot.}} \approx 10$ mrad. Responsible for the overall resolution then exclusively is the number of detected Cherenkov photons N through

$$\sigma_{\text{tot}} = \frac{\sigma_{\text{s.phot.}}}{\sqrt{N}},$$

which is simple count statistics. This number N has to be estimated and depends on

- the number of generated photons

$$N_0 = 2\pi \cdot \alpha \cdot L\left(\frac{1}{\lambda_{\text{min}}} - \frac{1}{\lambda_{\text{max}}}\right) \cdot \sin^2\theta_C = 2\pi \cdot \alpha \cdot L\left(\frac{1}{\lambda_{\text{min}}} - \frac{1}{\lambda_{\text{max}}}\right) \cdot \left(1 - \frac{m^2 + p^2}{p^2 \cdot n^2}\right) \tag{16}$$

  with parameters

  - fine structure constant α
  - trajectory length L in the radiator material

631 – mass and momentum m and p of the incident track
632 – wave length region $\lambda_{\min}$ and $\lambda_{\max}$ where the photon detector is sensitive and
633 – refraction index n

634 • the trapping fraction r_{trap} which is the fraction of the photons kept in the radiator/lightguide
635 due to total reflection and

636 • the detection efficiency ϵ of the photon detector, e.g. a photo multiplier tube (PMT)

637 In order to derive the path length L in the material one has to distinguish between the different
638 Cherenkov devices.

639 In case of the **Barrel DIRC** on first of all has to compute the curvature due to the motion of a
640 charged particle in a magnetic solinoidal field $B = B_z$. The radius r of the circular shape in (x, y)
641 projection is given by

$$r = \frac{p_t}{q \cdot B} = \frac{3.3356 \cdot p_t \text{ [GeV/}c\text{]}}{B \text{ [T]}}. \tag{17}$$

642 for a particle with charge $q = \pm e$ and transverse momentum $p_t = p \cdot \sin\theta$. Based on this one can
643 calculate the entering angle ψ in ϕ direction to

$$\psi = \arccos \frac{r_B}{2 \cdot r} \tag{18}$$

644 with r_B being the radius of the DIRC Barrel i.e. the distance between the bars and the beam
645 line. Here it is obvious that particles with $2 \cdot r < r_B$ will not hit the detector at all defining a
646 minimum transverse momentum $p_{t,\min}$. The path length after some geometrical considerations
647 then computes to

$$L \approx d_{\text{bar}} \cdot \sqrt{\frac{1}{\sin^2\theta} + \frac{1}{\tan^2\psi}} \tag{19}$$

648 where d_{bar} is the thinkness of the radiator bars and θ the dip angle of the helix of the track. The
649 expression is an approximation because curvature within the bar has been neglected. This leads
650 to significant wrong values for particles with $2 \cdot r \approx r_B$.

651 For the **Disc DIRC** and the **RICH** computing the radiator path length is much simpler. Here
652 L only depends on the dip angle and the radiator thinkness d_{rad} resulting in

$$L = \frac{d_{\text{rad}}}{\cos\theta}. \tag{20}$$

653 Also here no curvature within the radiators has been taken into account. This anyway would lead
654 to more complicated estimates since angular changes along the radiator path results in systematic
655 worsening of the Cherenkov angle which is neglected completely.

656 Finally we still need the trapping fraction r_{trap} to determine the number of detected photons. There
657 is no known analytic expression to compute this, thus 2 dimensional lookup tables $r_{\text{trap}}(\theta, p)$ for
658 every particle species have been prepared. Figure 22 shows as an example the trapping fraction
659 in the Barrel DIRC bars for muons and protons as a function of momentum p and dip angle θ.

660 With the path length L one can evaluate expression (16) so that the detected number of photons
661 can be estimated to

$$N = N_0' \cdot \epsilon \cdot r_{\text{trap}} \tag{21}$$

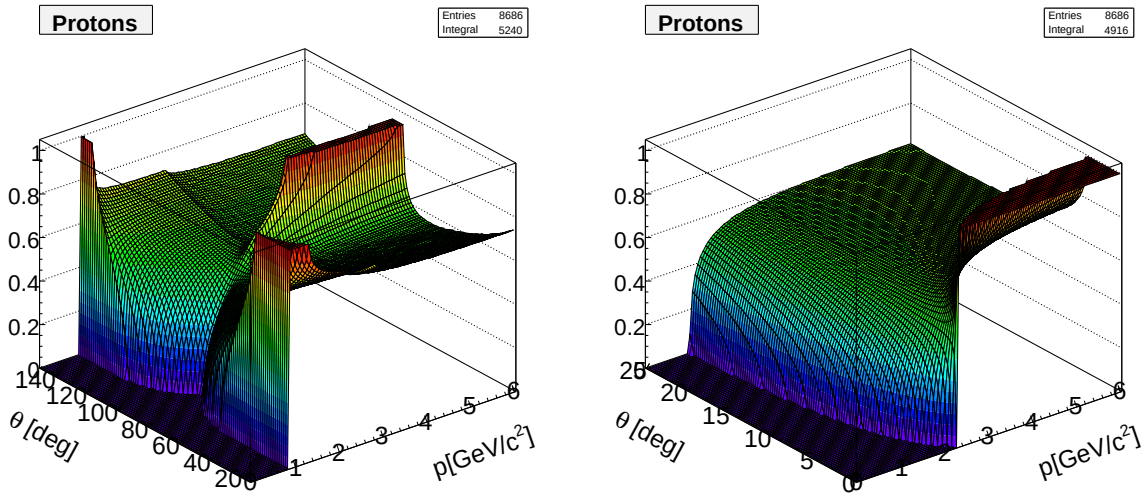

Figure 22: 2-dimensional picture of the trapping fraction for protons in the Barrel DIRC (left) and the Disc DIRC as a function of momentum p and dip angle θ.

where the N_0' is randomly generated from Poisson distibution with input value $\lambda = N_0$. This directly leads to the expected resolution σ_{tot} which is taken as the absolute uncertainty of the measurement of the Cherenkov angle. The simulated measured Cherenkov angle thus has been computed with formula (15) to

$$\theta_{C,\text{sim}} = \theta_C + \delta\theta_C \tag{22}$$

with randomly chosen value $\delta\theta_C$ from a gaussian distribution $G(\mu = 0, \sigma_{\text{tot}})$.

4.8 Time Of Flight Parametrization

From the geometrical point of view the calculation of the expected time of flight of a particle has similarities to the considerations done in 4.7 for the Barrel DIRC, since the TOF detector has also cylindrical shape. This requires also the particles with curvatures given by equation (17) to have a minimum transverse momentum p_t to reach the detector and produce a signal.

In order to compute the time of flight $t_{\text{TOF}} = s/v$ one in principal only needs the traveled distance s and the velocity v of the particle. While the latter one is simple to get by via the particles $\beta = p \cdot c/E$, the distance is not so easy to calculated due to the tracks curvature in the magnetic field. Nevertheless the calculation can be simplified exploiting the fact that the particles motion in z direction is independent of that one in th (x, y) plane. Therefore t can also be calculated via the ratio of the travelled angle Φ and the angular velocity ω

$$t_{\text{TOF}} = \frac{\Phi}{\omega} = \frac{1}{\omega} \cdot 2 \arcsin \frac{r_B}{2r} \tag{23}$$

with the determination of Φ illustrated in fig. 23. The angular velocity in the projected plane is given by

$$\omega = \frac{B}{3.3356 \cdot E} \tag{24}$$

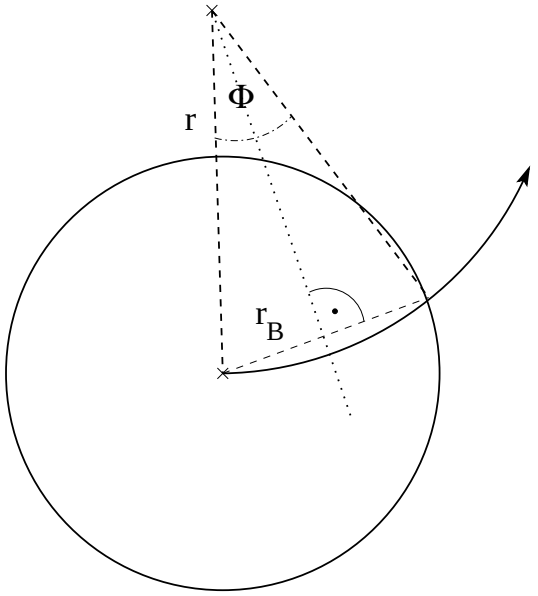

Figure 23: Projection of particle trajectory to (x, y) plane in order to determine Φ.

for a magnetic field B [T] and E [GeV]. With these expressions one can derive the true expected time of flight. What now has to be simulated is the expected accuracy of the measurement achieved by the detector. This depends on the time resolution assumed to be $\sigma_t \approx 100$ ps on one hand and on the resolution connected to track reconstruction on the other hand since the transverse momentum $p_t = p \cdot \sin(\theta)$ is needed to compute the flight length. Only a relative uncertainty $\sigma_p = \delta p/p \approx 2\%$ for the reconstructed absolute value of the momentum has been taken into account with respect to this, neglecting errors in polar angle measurement.

This results in measured values

$$t'_{\mathrm{TOF}} = t_{\mathrm{TOF}} + \delta t \tag{25}$$
$$p' = p \cdot (1 + \delta p) \tag{26}$$

with gaussian distributed deviations δt and δp according to $G(\mu = 0, \sigma_t)$ and $G(\mu = 0, \sigma_p)$. The primes denote from now the 'measured' or 'simulated' quantities. Now one basically has to reverse the process from above to get the simulated reconstructed value for the energy E needed to compute the squared mass

$$m'^2 = E'^2 - p'^2 \tag{27}$$

which acts as the observable of the TOF detector. Starting point is eq. (24) which forms to $E' = B/(3.3356 \cdot \omega')$ etc. The resulting term depending only on the quantities t'_{TOF}, p' and θ looks like

$$m'^2 = \left(\frac{B \cdot t'_{\mathrm{TOF}}}{2 \cdot 3.3356 \cdot \arcsin\left(\frac{r_B}{2 \cdot 3.3356 \cdot p' \sin(\theta)}\right)} \right)^2 - p'^2 \tag{28}$$

5 Evaluation

5.1 Potential of the Subsystems

5.2 Matching of the Subsystems

6 Global PID Scheme

The PANDA spectrometer will feature a complete set of innovative detectors for particle identification. The detection of neutral particles will be performed by a highly granular electromagnetic calorimeter. Charged particles will be identified in the low momentum region by their energy deposit and ToF, in all other momentum regions by innovative DIRC detectors. The target spectrometer will be complemented by a forward spectrometer to detect high momentum particles and surrounding muon detectors. Each detector systems performance is optimised in itself. Studies have begun to combine the responses of various detectors in a common framework based on a likelihood scheme or a carefully trained neutral network. These combined likelihood schemes are successfully employed at various detector systems like HERMEs, Belle and BaBar. They rely on a reliable parametrisation of the detector component response from simulation and test-beams. This has to be taken into account in testing PANDA's individual components. The combined performance of the system will be significantly better than the individual separation powers.

7 Conclusion

8 Acknowledgments

Thanks to analyzers from the "$\bar{\text{P}}$ANDA Physics Book", and all who help with their work and expertise to the success of the PID TAG.

This work is supported by EU FP6 grant, contract number 515873, DIRACsecondary-Beams.

References

[1] $\bar{\text{P}}$ANDA Collaboration, Technical Progress Report, FAI R-ESAC/Pbar 2005

[2] http://panda-wiki.gsi.de/cgi-bin/viewauth/Tagpid/WebHome, Wiki page of the $\bar{\text{P}}$ANDA PID TAG

[3] R. Aleksan et al., Nucl. Inst. Meth. **A397**, 261 (1997)

[4] A. Galoyan, V.V. Uzhinsky, AIP Conf. Proc. 796, pp. 79-8 2, 2005

[5] P. Schönmeier et al., to appear in the proceedings of 6th In ternational Workshop on Ring Imaging Cherenkov Counters (RICH 2007), Trieste, It aly, 15-20 Oct 2007.

[6] W.-M. Yao et al. 2006 J. Phys. G: Nucl. Part. Phys. **33** 1

[7] T. Akesson et al, CERN-PPE/94-140

9 Appendix

Members of the PID TAG

- G. Schepers, C. Schwarz - Barrel Dirc (Chairs)
- B. Kopf, R. Novotny - Barrel Calorimeter
- B. Seitz - Cherenkov Counter (Global PID)
- O. Denisov / M. P. Bussa - Muon Counter
- K. Föhl / P. Vlasov - Forward Cherenkov
- J. Smyrski / O. Wronska - Forward Calorimeter
- Q. Weitzel / S. Neubert - Time Pjection Chamber
- C. Schwarz, A. Galoyan - Time of Flight
- K. Götzen - Fast Simulation
- K. Peters - Physics